

## Article

# Study on Ground Experimental Method of Stagnation Point Large Heat Flux of Typical Sharp Wedge Leading Edge Structure

Ri Wang<sup>1</sup>, Fengfei Lou<sup>1,\*</sup>, Bin Qi<sup>2,\*</sup>, Rong A<sup>2</sup>, Yuanye Zhou<sup>1</sup>  and Sujun Dong<sup>1</sup>

<sup>1</sup> School of Aeronautical Science and Engineering, Beihang University, Beijing 100191, China; wr3705@163.com (R.W.); yuanye\_zhou@buaa.edu.cn (Y.Z.); dsj@buaa.edu.cn (S.D.)

<sup>2</sup> Qian-Xuesen Laboratory of Space Technology, China Academy of Space Technology, Beijing 100094, China; ivory\_118@126.com

\* Correspondence: lloufengfei@163.com (F.L.); qionline@163.com (B.Q.); Tel.: +86-1881-0257-526 (F.L.)

**Abstract:** In this paper, aimed at the problem of large temperature gradient thermal testing with the typical sharp wedge leading edge structure of a hypersonic vehicle, a subsonic high-temperature combustion gas heating (SHCH) test device is used to conduct a series of experiments on the heat flux simulation ability of subsonic high-temperature combustion gas in the stagnation point region. Firstly, for a hypersonic vehicle with a flying height of 24 km and Mach number range of 4~6.5, the stagnation point heat flux in the head area is obtained by numerical calculation of a typical leading edge structure, which is used as the experimental target of the thermal structure test. Secondly, an experimental specimen with a Gardon heat flux meter is designed with the same shape and size as the specimen in the numerical simulations to prepare for the subsequent SHCH test. Thirdly, a method to determine the combustion gas temperature based on a Kriging surrogate model is proposed. CFD numerical simulation is conducted using the SHCH test model, and the numerical calculation results are used as the training dataset. The Kriging surrogate model is used to establish an approximate fitting relationship between the stagnation point heat flux and experimental parameters under SHCH conditions. The corresponding combustion gas temperature values are found, respectively, with the hypersonic aerodynamic heat flux at Mach 5.0~5.4 as the target value. Finally, stagnation point heat flux testing of low-speed and high-temperature combustion gas is performed at different combustion gas temperatures. The experimental and target values obtained from hypersonic aerodynamic thermal simulations are compared and analyzed to verify the heating capacity of SHCH and the feasibility of hypersonic aerothermal simulation testing.

**Keywords:** hypersonic vehicle; sharp wedge; stagnation-point; large heat flux; CFD numerical simulation; ground experimental method



**Citation:** Wang, R.; Lou, F.; Qi, B.; A, R.; Zhou, Y.; Dong, S. Study on Ground Experimental Method of Stagnation Point Large Heat Flux of Typical Sharp Wedge Leading Edge Structure. *Aerospace* **2023**, *10*, 871. <https://doi.org/10.3390/aerospace10100871>

Academic Editor: Roberta Fusaro

Received: 25 August 2023

Revised: 25 September 2023

Accepted: 27 September 2023

Published: 6 October 2023



**Copyright:** © 2023 by the authors. Licensee MDPI, Basel, Switzerland. This article is an open access article distributed under the terms and conditions of the Creative Commons Attribution (CC BY) license (<https://creativecommons.org/licenses/by/4.0/>).

## 1. Introduction

To reduce aerodynamic drag, the sharp wedge structure composed of a small head radius cylinder and flat rear area is widely used in the nose cone, wing, and inlet leading edge of hypersonic vehicles [1–9]. Under hypersonic flight conditions, a large temperature gradient is formed along the direction of the airflow, and a large thermal stress is generated in the high-temperature area of the front end of the sharp wedge structure, which makes the front end of the wedge structure face a serious problem of excessive stress, and full-scale thermal testing of the structure is needed [10–18]. However, the traditional quartz lamp and graphite heating equipment are limited by their heating materials, and there are shortcomings in simulating temperature or continuous working time [19–24]. In addition, the operating cost of arc wind tunnels is very high, so gas flow wind tunnel testing is a good choice for conducting thermal tests [25–29].

The idea of a subsonic high-temperature combustion gas heating (SHCH) method is proposed in references [30–32], that is, the hypersonic gas velocity decreases and the temperature increases after passing through the shock wave, so the subsonic high temperature

combustion gas in the boundary layer can be used to simulate aerodynamic heat. At the same time, low-speed and high-temperature combustion gas has the characteristics of high power, long working time, good transient adjustment characteristics, and is economical, which can provide an effective solution for the thermal testing of large-size components in hypersonic vehicles.

On this basis, a new thermal test method is put forward for a combined heating method of high- and medium-temperature double subsonic airflow, which consists of a central subsonic high-temperature airflow passing through a small nozzle with the same diameter as the tip of the wedge surrounded by a medium-temperature airflow on both sides [30].

Numerical simulations show that the dual air channels affect the heat flux of the head cylinder region and rear plate region, respectively, which means that the head cylinder region is heated by the central high-temperature airflow and the plate region is heated by the medium-temperature airflow surrounded on both sides. They have little interference with each other. Thus, this new combined heating method can meet the requirements of large temperature gradient simulation of a wedge structure by adjusting the temperature of the dual airflow, respectively.

Considering that there are currently no conditions for dual-channel thermal simulation experiments, it is only verified through experiments in this paper that the central subsonic high-temperature airflow can satisfy the heat flux at the stagnation point head of the sharp wedge under hypersonic conditions. In this paper, the feasibility of the SHCH method is studied through the following four steps. In addition, it should be noted that the main purpose of this paper is to use high-temperature and low-speed gas flow to simulate hypersonic aerodynamic heat, that is, the heat flux of the sharp wedge head is the most important index. Therefore, in the numerical simulations in this paper, whether hypersonic or ground test CFD numerical simulation, the stagnation point heat flux of the sharp wedge head is the focus of attention, while the velocity gradient in the boundary layer, pressure, enthalpy, and other parameters are not recorded and discussed. During the actual test, the Mach number could only reach 5.4, so too many complex chemical effects are not taken into account.

Firstly, for a hypersonic vehicle with a flying height of 24 km and Mach number range of 4~6.5, the stagnation point heat flux in the head area is obtained by numerical calculation of the typical leading edge structure, which is used as the experimental target of thermal structure testing.

Secondly, a SHCH experimental device is designed that can realize the continuous and rapid adjustment of the combustion gas temperature in a wide range of 800 K to 2100 K through two-stage combustion and two-stage atomization. The experimental specimen with a Gardon heat flux meter is designed with the same shape and size as the specimen in the numerical simulations.

Thirdly, the Kriging surrogate model of the combustion gas heat flux obtained through CFD numerical simulation is adopted to determine the combustion gas temperature and mass flow under the SHCH experiment, with the aerodynamic heat flux taken as the objective heat flux.

Finally, the test is performed at different combustion gas temperatures. Through the stagnation point heat flux testing of low-speed and high-temperature combustion gas, the experimental values and stagnation point heat flux values obtained from the hypersonic aerodynamic thermal simulations are compared and analyzed to verify the heating capacity of SHCH and the feasibility of hypersonic aerothermal simulation testing.

## **2. CFD Numerical Simulation of the Sharp Wedge under Hypersonic Aerodynamic Heating**

### *2.1. Computational Domain and Boundary Conditions*

For the CFD numerical simulation of a sharp wedge under aerodynamic heating, the typical sharp wedge structure with a cylindrical head used by the American X-43 vehicle

is taken as the test target. The curvature radius of the stagnation point of the head and the angle of the triangular prism are  $3\text{ mm}$  and  $12^\circ$ , respectively, and the length along the airflow direction is  $139\text{ mm}$ . The half-symmetrical computational domain is shown in Figure 1, in which the green area is the airflow area, that is, the aerodynamic heating area. Figure 1a–c shows the test specimen, boundary conditions, and computational domain, respectively. The dimensions of the geometric model of the sharp wedge and the calculation domain are shown in Figures 2 and 3, respectively.

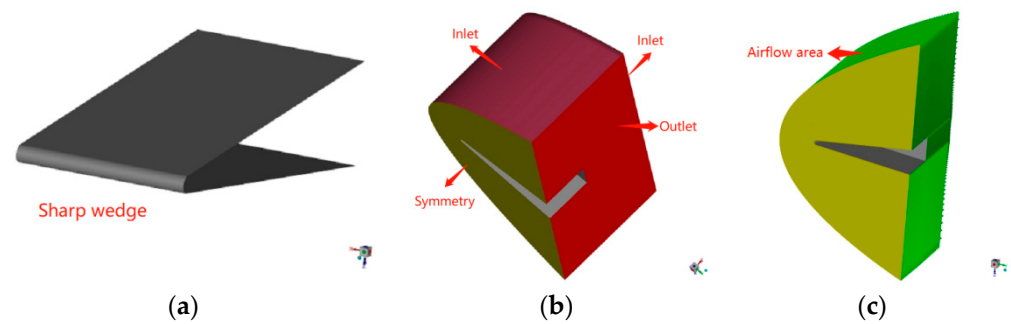


**Figure 1.** The half-symmetrical computational domain: (a) test specimen; (b) boundary conditions; (c) computational domain.

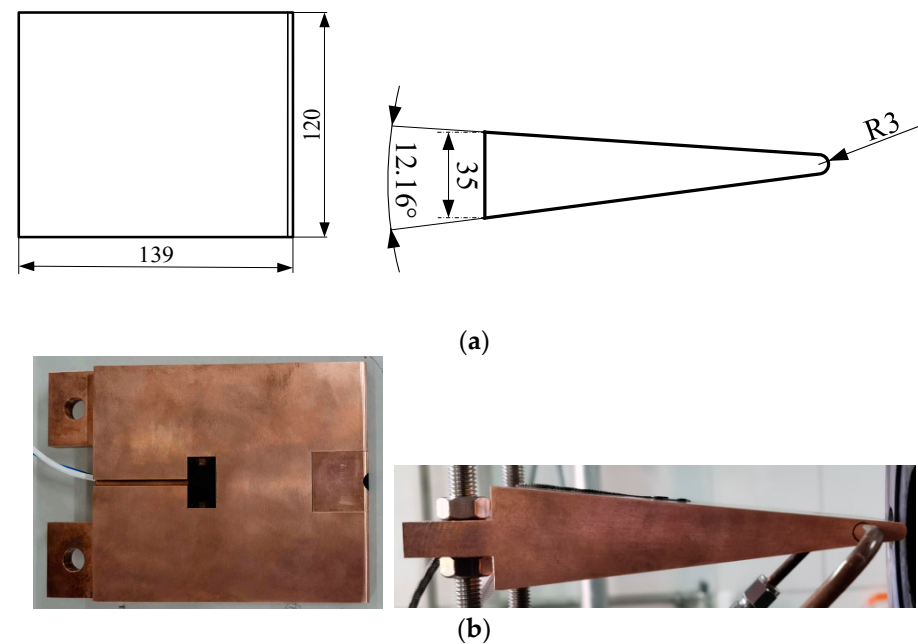


**Figure 2.** Dimensions of the geometric model of the sharp wedge specimen (unit is mm): (a) model diagram of sharp wedge; (b) physical map of sharp wedge.

First, the cold wall heat flux of the sharp wedge flying at different Mach numbers from 4 to 6.5, respectively, is calculated with a wall temperature of 300 K. The inlet boundary of the calculation model is set as the velocity inlet of different Mach numbers with a pressure of 2931 Pa and temperature of 220.65 K, according to the atmospheric parameters at a height of 24 km. The outlet boundary is set as the pressure outlet.

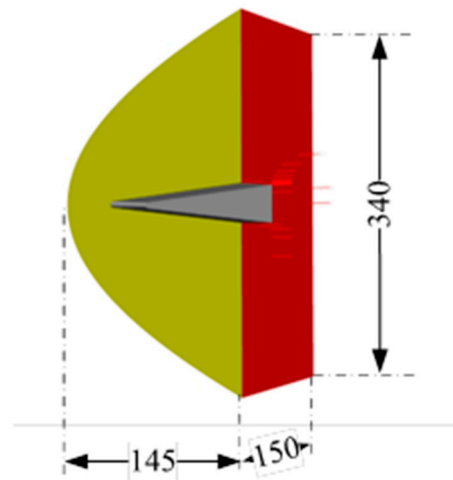


Figure 3. Dimensions of the geometric model of the computational domain (unit is mm).

In order to improve the accuracy of the numerical calculation, the variation in physical parameters with temperature must be considered. The specific heat capacity  $C_p$ , thermal conductivity  $\lambda$ , and dynamic viscosity  $\mu$  are calculated through a fitting function of temperature from 373 K to 3273 K, as shown in Formulas (1), (2), and (3), respectively. For Formulas (1)–(3), the physical parameters of air are selected from the study by Tao et al. [33].

$$C_p = 1161.482 - 2.369 \times T + 0.015 \times T^2 \quad 373K \leq T \leq 1273K \tag{1}$$

$$C_p = -7069.814 + 33.706 \times T - 0.058 \times T^2 \quad 1273K \leq T \leq 3273K$$

$$\lambda = 0.002 + 8.255 \times 10^{-5} \times T \tag{2}$$

$$\mu = \mu_0 \times \left(\frac{T}{273.15}\right)^{\frac{3}{2}} \times \left(\frac{273.15 + T_S}{T + T_S}\right) \tag{3}$$

where  $T$  is the temperature,  $\mu_0$  is the dynamic viscosity at one-atmosphere pressure and temperature of 273.15 K, and  $T_S$  is the Sutherland constant.

### 2.2. Governing Equations and Numerical Methods

Taking the calculation model under aerodynamic heating as an example, the mass, momentum, and energy conservation equations are shown as follows:

$$\frac{\partial \rho}{\partial t} + \nabla \cdot (\rho \vec{U}) = 0 \tag{4}$$

$$\frac{\partial (\rho \vec{U})}{\partial t} + \nabla \cdot (\rho \vec{U} \vec{U}) = \nabla P + \nabla \cdot (\tau) \tag{5}$$

$$\frac{\partial (\rho T)}{\partial t} + \nabla \cdot (\rho T \vec{U}) = \nabla \cdot \left(\frac{\lambda}{C_p} \nabla T\right) \tag{6}$$

where  $\rho$  is the density,  $t$  is the time,  $\vec{U}$  is the velocity in the  $x$ ,  $y$ , and  $z$  directions,  $P$  is the pressure, and  $\tau$  is the shear stress.

It is necessary to know the velocity field in order to solve the temperature field in Equation (6), which relies on first solving Equations (4) and (5). In this paper, ICEM commercial software is used to generate the mesh, and Equations (4)–(6) are solved using Fluent 2021 R2 commercial software. The mass, momentum, and energy conservation equations are discretized using the second-order upwind scheme. The iterative process is ended when the residuals of Equations (4)–(6) are less than  $1.0 \times 10^{-8}$ .

### 2.3. Grid Independence Verification

When the Mach number is 5, the variation in stagnation point heat flux with the number of grids is shown in Figure 4, and the grid heights of the first layer corresponding to different grid numbers are shown in Table 1. It can be seen that when the number of grids is above 5.69 million, the stagnation point heat flux will no longer change with an increase in the number of grids. In the numerical calculation of hypersonic aerodynamic heat, the height of the first-layer grid near the wall is very high. Bibhab et al. [33] performed simulation calculations on the aerodynamic heat of the stagnation point and the requirements of the first grid, finding that the height of the first grid greatly influenced the calculation results of heat flux, especially the stagnation point heat flux.

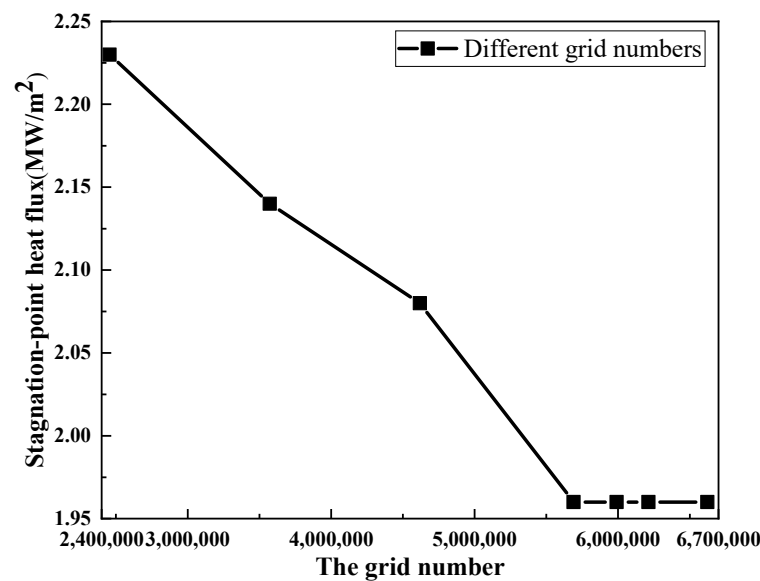


Figure 4. The variation in stagnation point heat flux with the number of grids.

Table 1. Mesh parameters.

Grid Number (Million)	Grid Height of the First Layer (mm)
2.456	0.05
3.573	0.02
4.619	0.01
5.690	0.007
5.990	0.005
6.212	0.002
6.623	0.001

Here, it is necessary to mention the dimensionless parameter  $y^+$ , the definition of which is shown in Formula (1). The  $y^+$  value is considered to be the focus of attention because different first-level grid heights will have different  $y^+$  values. Figure 5 shows the  $y^+$  values of the specimen surface with three different grid numbers along the airflow direction. It can be seen from the figure that when the grid number is greater than 5.69 million, the  $y^+$  value is basically less than 1. Wang et al. [34] used Fluent 2021 R2 commercial software to perform hypersonic aerothermal calculations using a pressure-based solver and SST turbulence model, pointing out that the accuracy requirements of aerothermal calculations could be met when the value of  $y^+$  was kept less than 1. In this paper, the same method is

used to perform the calculations and the results are reliable. Therefore, the set with 6.212 million grids is finally selected for the CFD numerical simulation.

$$y^+ = \frac{u^* \times y}{\nu} \quad (7)$$

where  $u^*$  is the friction velocity near the wall, the distance between the first grid node and the wall, and  $\nu$  is the kinematic viscosity of the fluid.

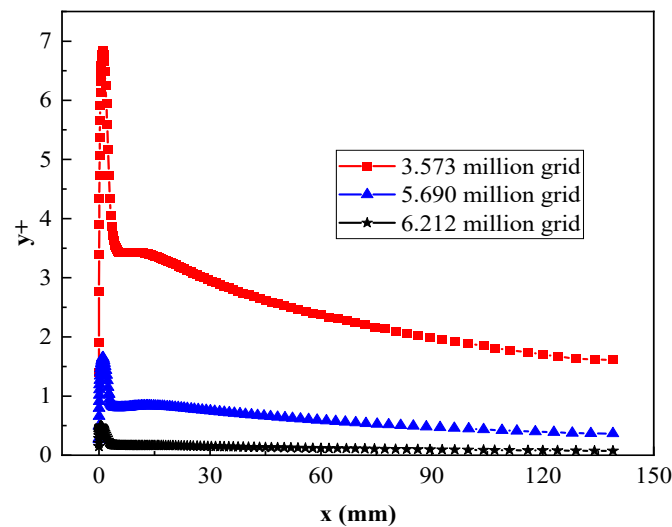


**Figure 5.** The  $y^+$  value of the specimen surface with different grid numbers along the airflow direction.

#### 2.4. Stagnation Point Heat Flux Simulation Target

The aerodynamic heat of a hypersonic vehicle with a sharp wedge leading edge structure at an altitude of 24 km and Mach number in the range of 4~6.5 Ma is numerically simulated. Figure 6 shows the static pressure and temperature distribution of hypersonic airflow around the tip wedge structure at a Mach number of 5, and Figure 7 shows the hypersonic aerodynamic heating flux density distribution at different Mach numbers with an isothermal wall condition of 300 K. The stagnation point heat flux is shown in Table 2.

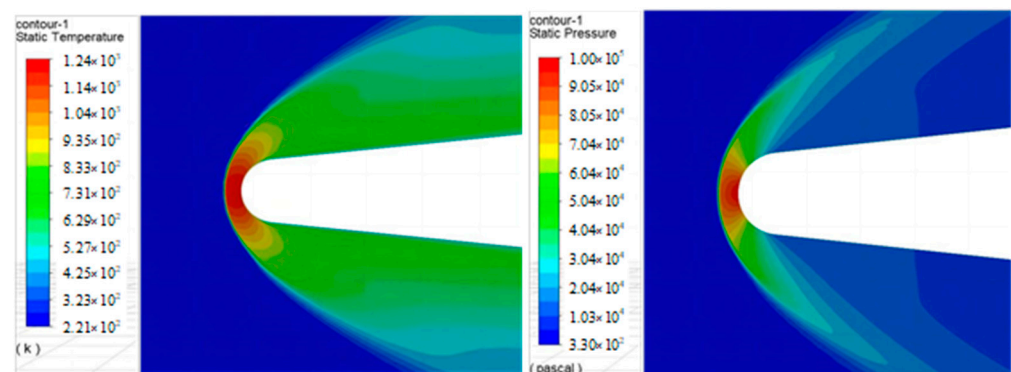


**Figure 6.** Static pressure and temperature distribution of hypersonic airflow around the tip wedge structure at Mach 5.

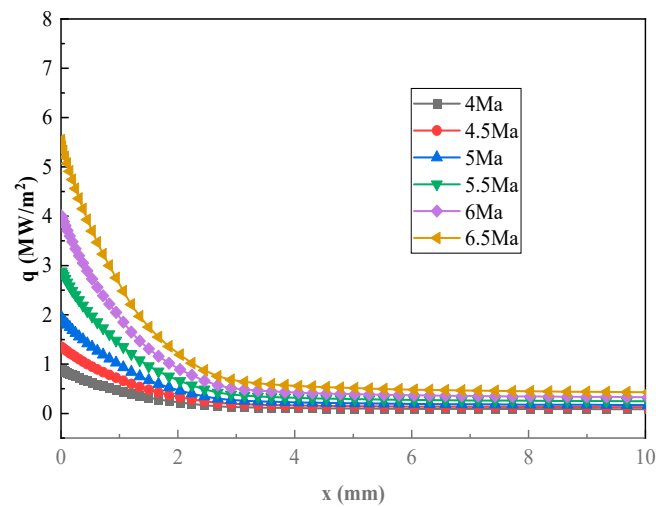


**Figure 7.** Hypersonic aerodynamic heating flux density distribution at different Mach numbers with an isothermal wall condition of 300 K.

**Table 2.** The stagnation point heat flux.

Mach Number	Stagnation Point Heat Flux (MW/m <sup>2</sup> )
6.5	5.54
6	4.02
5.5	2.86
5	1.98
4.5	1.35
4	0.88

It can be seen from the above results that the higher the Mach number, the higher the heat flux in the stagnation point region of the head, with little difference in the rear plate region. The heat flux of the head cylinder decreases rapidly with increasing distance from the stagnation point, and the higher the Mach number, the greater the change rate.

### 3. Experimental Device and Method

#### 3.1. Experimental Device

Figure 8 shows a flow chart of the subsonic high-temperature combustion gas heating (SHCH) test device described in reference [35], which is composed of a combustion gas generator (including an air equalizing chamber, primary combustor, and secondary combustor/mixer), measurement and control system, gas supply system, oil supply system, and cooling system.

Its working principle is that aviation kerosene and air are used as the fuel and oxidant, respectively. After combustion, high-temperature combustion gas is generated, and a uniform and stable temperature field is formed in the test section of the hot wind tunnel. The gas supply system is divided into the following three branches, namely the atomization branch, the primary combustion branch, and the secondary combustion/mixing branch. At the same time, cooling water is used to cool the combustor, so that the device is operated within a safe range.

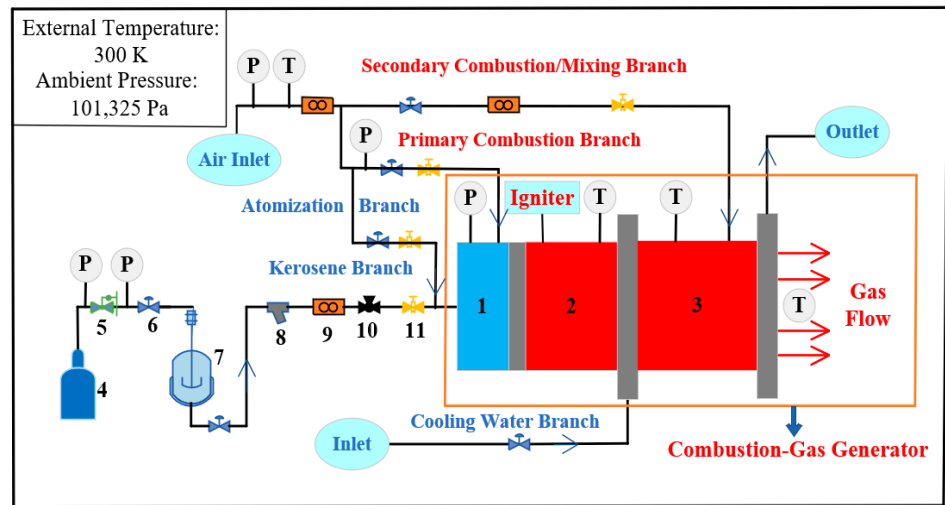


**Figure 8.** The combustion gas wind tunnel device. 1. Air equalizing chamber; 2. Primary combustor; 3. Secondary combustor/mixer; 4. Nitrogen cylinder; 5. Pressure-reducing valve; 6. Manual valve; 7. Oil tank; 8. Filter; 9. Flow meter; 10. Proportional valve; 11. Solenoid valve.

Figure 9 shows the combustion gas generator and measurement and control system of the test system. It can be seen also from reference [35] that the test system can achieve continuous, stable, and ultra-wide linear adjustment of the combustion gas temperature from 1050 K to 2100 K, as shown in Figure 10.



**Figure 9.** The combustion gas generator and measurement and control system of the test system.

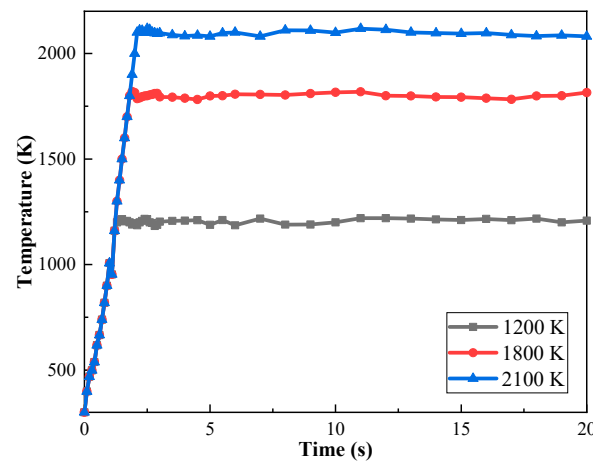


**Figure 10.** Fluctuation of outlet temperature at 1200 K, 1800 K, and 2100 K.

### 3.2. Experimental Specimen with Gardon Heat Flux Meter

Considering the convective heating condition, the heat flux in the stagnation point is closely related to the size of the geometrical structure of the specimen head. The experimental specimen and Gardon heat flux meter are shown in Figure 11, respectively, which are both made of copper. The shape and dimensions of the specimen shown in Section 2 “CFD numerical simulation of the sharp wedge under hypersonic aerodynamic heating” are the same as the sharp wedge described in Figure 2. The Gardon heat flux meter is constructed in a shape similar as that of the test specimen and finally installed in the middle of the head of the specimen. As shown in Figure 11a, the size ratio between the specimen in physical form and the specimen in the simulation calculation is 1:1, and the gap in the middle is used for the installation of the Gardon heat flux meter.

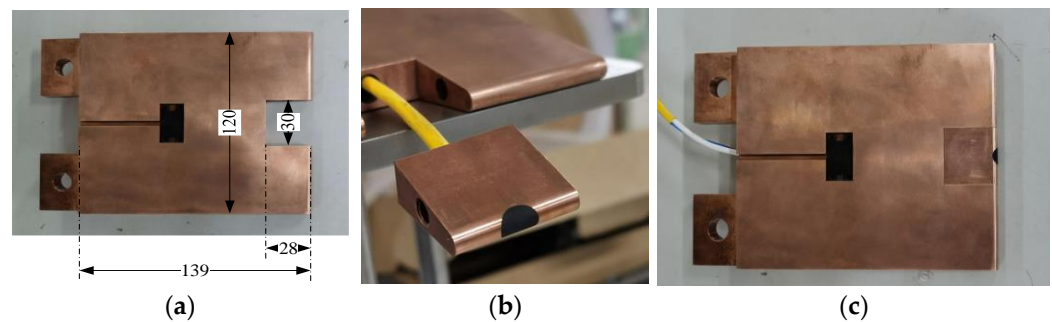


**Figure 11.** The test specimen and Gardon heat flux meter: (a) test specimen; (b) Gardon heat flux meter; (c) combined component.

The design range of the water-cooled Gardon heat flux meter is  $4000 \text{ kW/m}^2$ , and the three-dimensional structure design is shown in Figure 12. The induction surface of the round copper foil plate at the stagnation point is 2.7 mm in diameter and 0.24 mm in thickness. The surface is sprayed with black matte paint with an absorptance of about 0.95 and is consistent with the arc of the pointed wedge head. The water cooling channel uses side openings to cool the whole copper specimen, which enhances the high temperature resistance of the Gardon heat flux meter. The two ends of the water cooling channel are threaded to connect the cooling water pipe.

The structural profile near the copper foil induction surface of the Gardon heat flux meter is shown in Figure 13. The copper wire is welded in the center of the copper foil, and then the copper foil is welded on the copper heat sink. To simultaneously monitor the Gardon heat flux meter surface temperature, a B-type thermocouple is welded at the junction (inside side) of the copper foil and copper sink. A cylindrical hole is opened in the center of the circular foil along the axial direction to lead out the sensor signal line, and the other end is packaged with a specific structure and converted into a standard signal line connector.

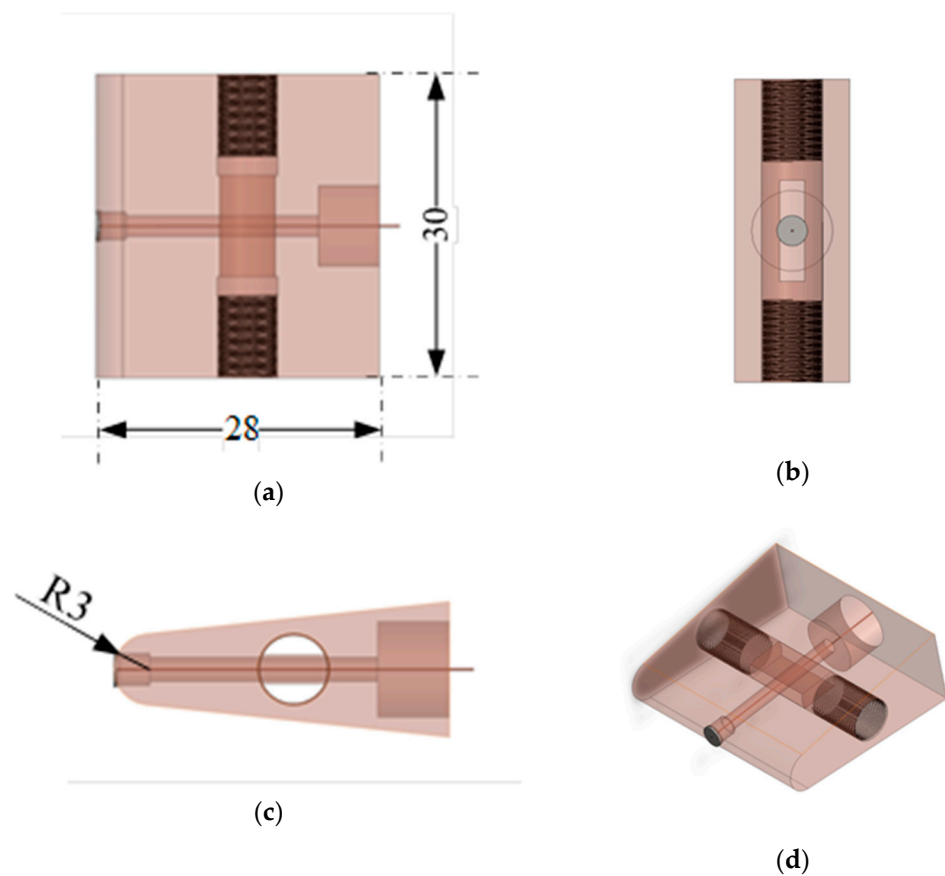


**Figure 12.** The three-dimensional structure design of water-cooled Gardon heat flux meter (unit is mm): (a) top view; (b) side view; (c) front view; (d) three-dimensional map.

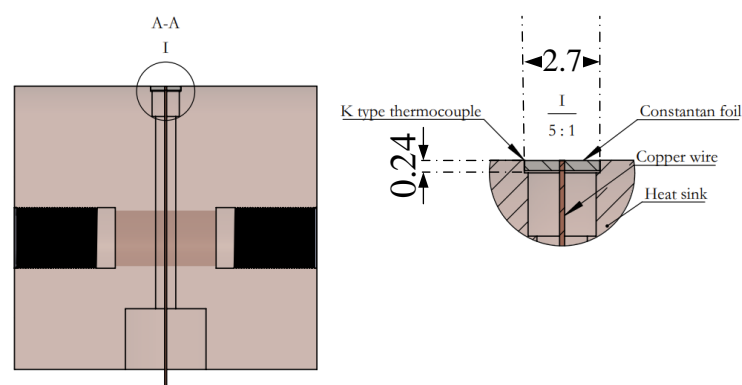


**Figure 13.** Gardon heat flux meter's copper foil induction surface structure profile (unit is mm).

The calibration device of the black-body furnace is used to calibrate the newly developed water-cooled Gardon heat flux meter with the standard Gardon heat flux meter, and the calibration system is shown in Figure 14. The standard Gardon heat flux meter (model no. 64-200-20) was manufactured by Medtherm Corp. (USA). The physical diagram of the sensor is shown in Figure 15. The measured values of the standard heat flux meter and output voltage values of the newly developed heat flux meter under the working condition of  $2000 \text{ kW/m}^2$  are shown in Figure 16. The average coefficient of the water-cooled Gardon heat flux meter was determined to be  $0.00305 \text{ mV}/(\text{kW/m}^2)$ , the maximum linear output range was  $4000 \text{ kW/m}^2$ , and the measuring accuracy was  $\pm 3\%$ .



**Figure 14.** The calibration system of the Gardon heat flux meter: (a) calibration system; (b) calibration test.

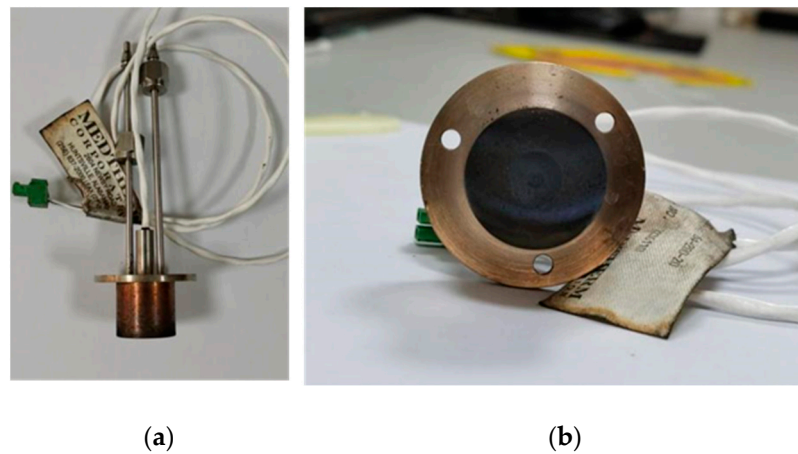


**Figure 15.** The standard Gardon heat flux meter: (a) standard Gardon heat flux meter; (b) inductive surface.

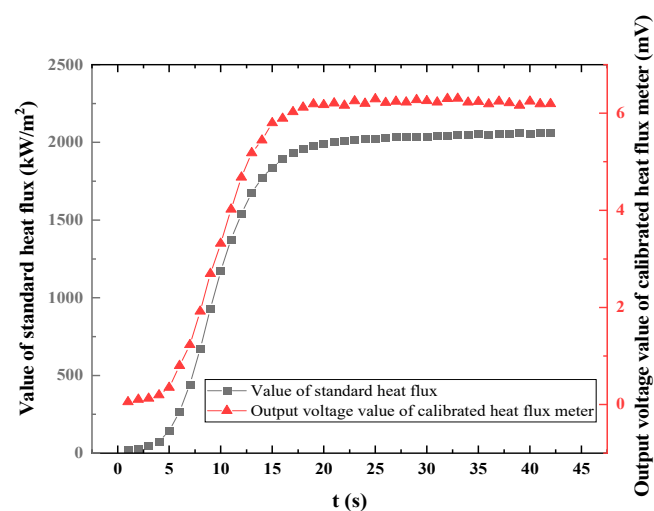


**Figure 16.** Value of standard heat flux meter and output voltage value of calibrated heat flux meter.

### 3.3. Experimental Specimen Installation

To avoid heating the heat flux meter and test piece in the process of gas flow temperature regulation, an electric slide rail is set in the vertical flow direction. The water-cooled Gardon heat flux meter, test piece, and gas flow temperature thermocouple are fixed at both

ends of the slide rail bracket, which is 200 mm away from the burner. Thus, in the process of gas temperature regulation, the thermocouple can be moved to the central position through the measurement and control system, and the heat flux meter specimen can be moved outside the heating range of the gas flow. When the temperature of the gas flow is stable, the heat flux meter specimen is moved to the center of the gas flow and the thermocouple is moved out of the heating range of the gas flow. The installation positions of the heat flux meter, test piece, and temperature thermocouple are shown in Figure 17, respectively.

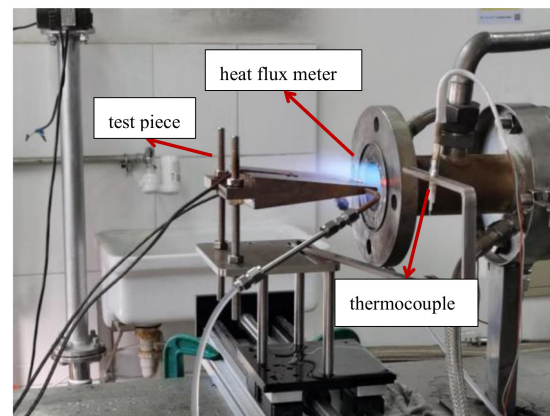


**Figure 17.** The installation positions of the heat flux meter, test piece, and temperature thermocouple.

### 3.4. Uncertainties of Experimental Parameters

The uncertainties of the experimental parameters were analyzed, and the specific data is shown in Table 3. Temperature sensors are arranged at the exit of the combustor to measure the combustion gas temperature, flow meters are used to measure the mass flow of air and aviation kerosene, and the Gardon heat flux meter is used to measure the stagnation point heat flux.

**Table 3.** Uncertainties of experimental parameters.

Sensor	Number	Accuracy	Full Scale	Model
Temperature	1	$\pm 1$ K	2100 K	B type
Flow meter	2	$\pm 0.2\%$ of full scale	180 g/s	Shouke
Gardon heat flux meter	1	$\pm 3\%$ of full scale	3 MW/m <sup>2</sup>	GD-4000
Recirculating cooler	1	$\pm 0.2\%$ of full scale	313 K	FLW2503
Data acquisition instrument	1	$\pm 0.2\%$ of full scale		HP34972A
Flattening oven	1	3%		HFC-3000

### 3.5. Experimental Method

To avoid fluctuations in combustion characteristics caused by changes in gas mass flow rate, a method of fixing the gas mass flow rate and adjusting the gas flow temperature is adopted to achieve different heating capabilities. Therefore, based on the maximum stable combustion flow rate of the SHCH test equipment, the air mass flow rate is set to 150 g/s when the parameters are determined by Kriging surrogate model in this paper. Then, by adjusting the fuel mass flow rate and changing the fuel gas ratio during the combustion process, the combustion gas temperature from 1200 K to 1800 K is generated to meet the demand for heat flux density.

The specific test process is as follows:

- ① Fixt the specimen with the water-cooled Gardon heat flux meter and temperature thermocouple on the slide rail support, respectively, with the height of adjustment

- consistent with the center position of the nozzle, as close as possible to the section of the nozzle;
- ② Start the chiller, with the water supply temperature of the cooling water at 4 °C. Start the measurement and control system, and set the sampling frequency of heat flow to 0.2 s/time;
  - ③ Debug the electric slide rail, first move the heat flux meter to the center of the airflow as the initial position, and then enter the command +200 mm to move the thermocouple to the center of the airflow;
  - ④ Open the high pressure air supply system, and adjust the air quality flow rate at 150 g/s;
  - ⑤ Start the combustion gas generator, keep the ignition state, and burn steadily for 60 s;
  - ⑥ Set the gas flow temperature control target, turn on the measurement and control system to automatically adjust the oil supply flow, and burn steadily for more than 30 s after reaching the control target;
  - ⑦ Input the sliding rail movement instruction so that the heat flux meter quickly reaches the experimental median. After 30 s, input the sliding rail movement instruction again, so that the heat flux meter moves back to the initial position and the thermocouple reaches the airflow center.
  - ⑧ Repeat steps 5 and 6 to complete a variety of gas flow temperature condition tests.
  - ⑨ Adjust the fuel flow to the ignition state, and when combustion is stable for over 60 s, close the oil supply valve so that the burner is extinguished, and stop data collection.

#### 4. Construction of the Kriging Surrogate Model

##### 4.1. Method Overview

The heat flux density at the stagnation point of a sharp wedge is related to experimental parameters, including the gas flow temperature and flow rate, under SHCH conditions. Whether the experimental heat flux is equivalent to the hypersonic aerodynamic heat (target heat flux) depends on the accuracy of the selected experimental parameters. To quickly and accurately determine the experimental parameters, it is necessary to establish the relationship between the experimental heat flux and experimental parameters.

In the absence of appropriate empirical formulas for the surface heat transfer coefficient, a Kriging surrogate model is constructed, which has lower computational cost while yielding results close to the numerical analysis results. The aim of the Kriging surrogate model is to build the relationship between the heat flux with various experimental parameters and identify suitable experimental parameters that correspond to the target heat flux.

The steps to determine the gas parameters based on the Kriging surrogate model are as follows:

- (1) Use the Latin hypercube sampling method to obtain sample points in the design space.
- (2) Under SHCH conditions, use the CFD numerical simulation to obtain the stagnation point heat flux density of the sharp wedge.
- (3) Use the Kriging surrogate model to construct an approximate fitting relationship between the design sample points and stagnation point heat flux. Analyze the accuracy of the constructed surrogate model, and if the accuracy is not satisfactory, reconstruct the model by increasing the number of sample points until the accuracy meets the requirements.
- (4) Take the specified hypersonic aerodynamic heat flux as the target value and solve for the corresponding experimental parameters.

#### 4.2. Obtaining Sample Points in the Design Space

The Latin hypercube design method is a stratified sampling approach that has the characteristics of spatial uniformity and good coverage [36]. The method of generating the Latin hypercube experimental design points is as follows:

$$x_p^{(i)} = \frac{\pi_p^{(i)} + U_p^{(i)}}{n} \tag{8}$$

where  $I$  represents the  $i^{\text{th}}$  experiment,  $p$  represents the  $p^{\text{th}}$  design variable,  $n$  is the number of sample points,  $\pi$  denotes the independent random permutation, and  $U$  represents a random number in the range  $[0, 1]$ .

The temperature range of the high-temperature gas flow is from 900 K to 2200 K, and the mass flow rate range is from 50 to 250 g/s. The Latin hypercube design method is used to generate 32 sample points, as shown in Figure 18.

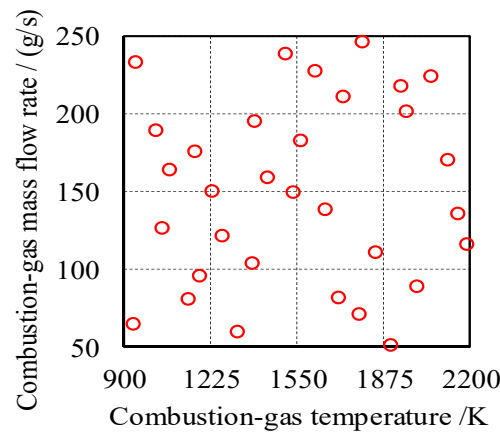


Figure 18. Distribution of sample points in the surrogate model.

#### 4.3. Generation of Stagnation Point Heat Flux by CFD Numerical Simulation

The CFD numerical simulation is applied to generate the stagnation point heat flux with the required variable space. For the CFD numerical simulation under combustion gas heating, the shape and size of the sharp wedge are unchanged, and the distance between the nozzle and sharp wedge and the radius of the nozzle in the calculation model are 100 and 28 mm, respectively, according to the experimental device. In the simulation process, the outer surface of the specimen is set to 300 K, and the final stagnation point heat flux is the 300 K cold wall heat flux. A quarter of the calculation model is shown in Figure 19, wherein the interior of the red area is the combustion gas heating area.

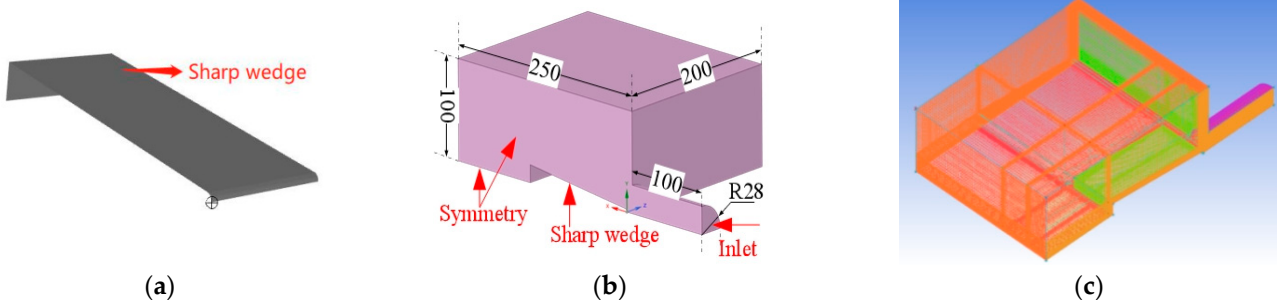


Figure 19. A quarter of the computational domain: (a) test specimen; (b) geometric diagram; (c) grid diagram.

Aviation kerosene is composed of hydrocarbon compounds of different fractions, with a molecular carbon–hydrogen ratio of 1:1.9184 and oil–gas ratio of 1:20. In the complete combustion state, the mass ratio of each component of combustion gas is shown in Table 4. In order to improve the accuracy of the numerical calculation, the variation in physical parameters with temperature must be considered. In addition, there is an issue that must be addressed. In the ground gas test and CFD numerical simulation, the composition of the gas produced by the mixture of kerosene and air combustion is completely different from that produced by the hypersonic vehicle flying in the air, but this issue is not considered and explored in detail in this article. The reason is mainly related to the main content of this paper, which mainly uses high-temperature and low-speed gas flow to simulate the aerodynamic heat of the sharp wedge head. Therefore, the heat flux density is an important index to be considered whether in a SHCH ground test, SHCH CFD numerical simulation, or hypersonic CFD numerical simulation. The specific heat capacity  $C_p$ , thermal conductivity  $\lambda$ , and dynamic viscosity  $\mu$ , are calculated by fitting the function of temperature from 273 K to 2100 K, as shown in Formulas (9), (10), (11), and (12), respectively. Formulas (9)–(12) represent physical property parameters of the combustion gas, which are obtained by fitting the data in reference [37].

$$C_p = 2.5768 \times 10^{-8} \times T^3 - 9.1631 \times 10^{-7} \times T^2 + 3.2362 \times 10^{-1} \times T + 947.34 \quad (9)$$

$$\lambda = 8.613 \times 10^{-5} \times T - 8.3514 \times 10^{-4} \quad (10)$$

$$\mu = -7.903710^{(-12)} \times T^2 + 4.4362 \times 10^{-8} \times T + 4.9955 \times 10^{-6} \quad (11)$$

$$\rho = 6.58 \times 10^{-13} \times T^4 - 3.54 \times 10^{-9} \times T^3 + 7.04 \times 10^{-6} \times T^2 - 6.34 \times 10^{-3} \times T + 2.54 \quad (12)$$

**Table 4.** Mass proportion table of combustion gas components.

Component	CO <sub>2</sub>	H <sub>2</sub> O	O <sub>2</sub>	N <sub>2</sub>
Mass proportion (%)	14.8	72.9	6.7	5.6

For the simulation of subsonic combustion gas flow heating, a pressure-based solution method can be adopted, and numerical solutions can be achieved through the pressure/velocity correction relationship. The turbulence model selects realizable  $k$ - $\epsilon$ , and enhanced wall treatment is selected as the wall function, keeping  $y^+$  around 1.

From Figure 20a, it can be seen that the heat flux results for 1.8 million grids are significantly different from those for 3.2 million and 4.4 million grids. When the number of grids increases to 3.2 million, an independent solution has been obtained, and increasing the number of grids has no significant impact on the calculation accuracy. Therefore, 3.2 million grids is selected for subsequent calculations. The  $y^+$  values along the surface of 3.2 million grids are all less than 1, as shown in Figure 20b, which meets the calculation requirements.

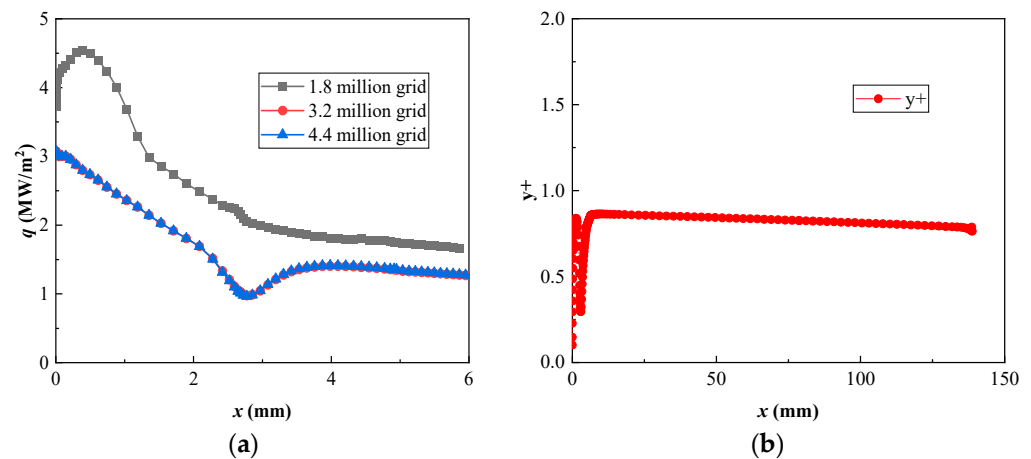


**Figure 20.** Verification of grid independence: (a) stagnation point heat flux with different grid numbers; (b) the  $y^+$  value along the upwind curve of the specimen with 3.2 million grids.

#### 4.4. Kriging Surrogate Model of Combustion Gas Heating Flux

The Kriging surrogate model is a method of linear optimization and unbiased interpolation of data samples. The Kriging surrogate model was chosen for three reasons. Firstly, the applicability of the Kriging surrogate model is extensive, which is suitable for linear and nonlinear mathematical models. The second reason is that the question in this paper is relatively simple, and the Kriging surrogate model can be applied to this question. Thirdly, in our research group, this model is widely used and has high accuracy. It can be expressed as [38]:

$$f(\mathbf{X}) = g(\mathbf{X}) + z(\mathbf{X}) \quad (13)$$

where  $g(\mathbf{X})$  is the global approximation of  $\mathbf{X}$ , and  $z(\mathbf{X})$  is a stochastic function that satisfies zero mean with  $\sigma^2$  standard deviation and nonzero covariance.

The covariance matrix of  $z(\mathbf{X})$  is expressed as:

$$\text{Cov}[z(\mathbf{X}_i), z(\mathbf{X}_j)] = \sigma^2 \mathbf{R}[R(\mathbf{X}_i, \mathbf{X}_j)] \quad (14)$$

where  $\mathbf{R}$  is the correlation coefficient matrix,  $R$  is the correlation function,  $i = 1, 2, \dots, n$ , and  $j = 1, 2, \dots, n$ , where  $n$  is the sample number.

Under the condition of a constant wall temperature at 300 K, the typical stagnation point cold wall heat flux density of the sharp wedge structure is obtained through CFD numerical simulation for the sample points. Using the Gaussian correlation function, the Kriging surrogate model is established for the cold wall heat flux density in the stagnation point of the sharp wedge structure within the design space.

#### 4.5. Uncertainty Analysis

Figure 21 presents the predicted results of the surrogate model within the design space and a comparison between the predicted values for four randomly selected test sample conditions and the results obtained from the CFD numerical simulation. In order to clarify the comparison, Table 5 also compares the predicted and calculated values. From the chart, it can be observed that the predicted values for the four test sample conditions closely match the results obtained from the CFD simulation, indicating that the constructed surrogate model exhibits a high level of predictive accuracy.

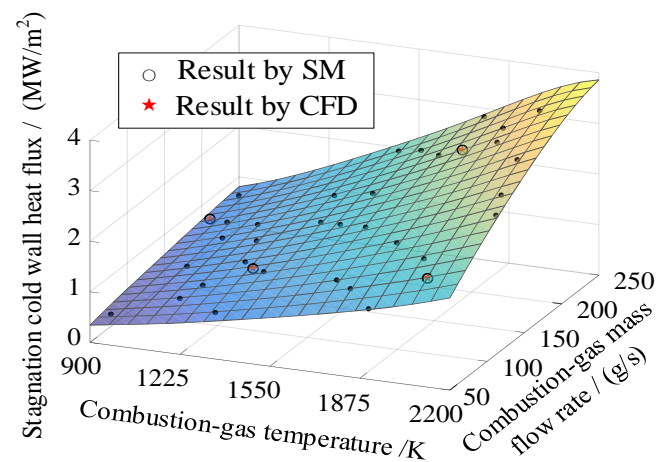


**Figure 21.** Prediction results of gas heating cold wall heat flux via the surrogate model.

**Table 5.** Comparison between predicted and calculated values.

Test Condition	Combustion Gas Temperature (K)	Combustion Gas Mass Flow (g/s)	Predicted Heat Flux of Surrogate Model (MW/m <sup>2</sup> )	Calculated Heat Flux Value of CFD (MW/m <sup>2</sup> )
1	930	200	0.7589	0.756
2	2064	70.6	1.8866	1.88
3	1328	110	1.0874	1.09
4	1821	210	2.6825	2.68

To quantitatively evaluate the accuracy of the surrogate model, the average relative error is defined.

$$e_p = \frac{1}{M} \sum_{m=1}^M \left| \frac{q_{\text{ROM}} - q_{\text{CFD}}}{q_{\text{CFD}}} \right| \quad (15)$$

where  $q_{\text{CFD}}$  is the stagnation point heat flux obtained from the CFD simulation,  $q_{\text{ROM}}$  is the predicted value from the surrogate model, and  $m = 1, 2, \dots, M$ , where  $M$  is the number of test samples.

The average relative error of the stagnation point heat flux for the four test samples is 0.27%, indicating a high level of accuracy. Therefore, there is no need to further increase the number of sample points.

## 5. Experimental Results and Discussion

### 5.1. Combustion Gas Temperature Determination Based on Kriging Surrogate Model

To avoid fluctuations in combustion characteristics caused by changes in combustion gas mass flow rate, this paper employed a method of fixing the combustion gas mass flow rate and adjusting the combustion gas flow temperature to achieve an aerodynamic thermally equivalent simulation. Consistent with the experimental conditions, the combustion gas mass flow rate was kept constant at 150 g/s.

Under aerodynamic heating conditions, at Mach numbers of 5.0, 5.1, 5.2, 5.3, and 5.4, the stagnation point cold wall heat flux values were obtained through numerical calculations. Using the cold wall heat flux as the target heat flux, the combustion gas temperature required for each condition was obtained based on the Kriging surrogate model under combustion gas heating conditions, as shown in Table 6.

**Table 6.** The target stagnation point heat flux and optimal SHCH test conditions.

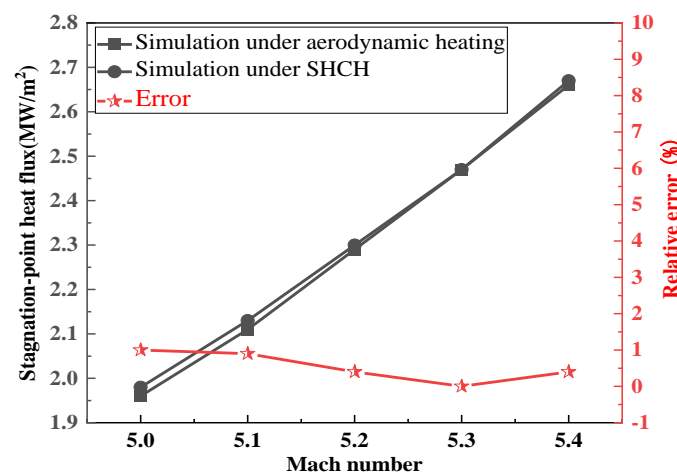
No.	Target Stagnation Point Heat Flux		Optimal SHCH Test Conditions Based on Kriging Surrogate Model		
	Mach Number	Stagnation Point Cold Wall Heat Flux (MW/m <sup>2</sup> )	Combustion Gas Mass Flow (g/s)	Combustion Gas Temperature (K)	Mach Number
1	5.0	1.96	150	1697	0.36
2	5.1	2.11	150	1764	0.37
3	5.2	2.29	150	1844	0.38
4	5.3	2.47	150	1923	0.39
5	5.4	2.66	150	2008	0.40

The Mach number of the combustion gas flow was calculated by the combustion gas mass flow rate of 150 g/s, according to the calculation formula shown in Equation (16):

$$Ma = \frac{m}{\rho A \sqrt{\gamma R_g T}} \quad (16)$$

where  $m$  is the combustion gas mass flow rate ( $m = 150$  g/s),  $\rho$  is the combustion gas density. (At five different combustion gas temperatures, the density is fitted according to Equation (11).),  $A$  is the cross-section area of the nozzle ( $A = 3.14 \times 0.028 \times 0.028 = 0.00246$  m<sup>2</sup>),  $\gamma$  is the combustion gas specific heat ( $\gamma = 1.33$ ),  $R_g$  is the gas constant ( $R = 287$  J/(kg·K)), and  $T$  is the combustion gas temperature ( $T = 1697$  K, 1764 K, 1844 K, 1923 K, and 2008 K).

To validate the accuracy of the obtained combustion gas flow temperatures based on Kriging surrogate model, CFD numerical simulation was conducted using the combustion gas flow temperatures as boundary conditions to obtain the stagnation point heat flux under SHCH conditions. The results were compared with the aerodynamic heating stagnation point heat flux (target heat flux), as shown in Figure 22. From Figure 22, it can be observed that the stagnation point heat flux obtained from the two heating methods was nearly identical and the maximum relative error was 1%, indicating that the surrogate model accurately provided the required gas flow temperatures for aerodynamic thermal simulation testing. This also demonstrated that the SHCH simulation could effectively simulate the aerodynamic heated environment of hypersonic vehicles and meet the requirements for simulating the stagnation point heat flux of vehicles under hypersonic conditions.

**Figure 22.** Comparison of simulated values under aerodynamic heating and SHCH.

### 5.2. Experimental Results

During the test, the combustion gas temperature and value of heat flux at the stagnation point under stable combustion conditions were collected, as shown in Figure 23. As mentioned earlier, the two parameters were measured alternately, which meant that the

heat flux density and gas flow temperature sensors took turns entering the heating area and were controlled by sliding rails to avoid burning out.

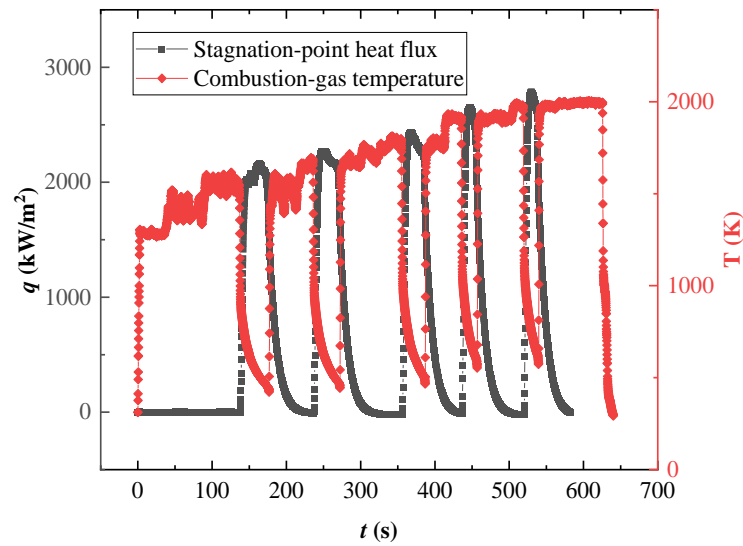


Figure 23. Combustion gas temperature and stagnation point heat flux.

During the experiment, the surface temperature of the Gardon heat flux meter installed at the head of the specimen continuously increased due to gas heating. The measured data of the heat flux meter corresponded to the convective heat transfer intensity between the given gas flow and its high-temperature wall. The cold wall heat flux of 300 K was observed by conversion based on an equal convective heat transfer coefficient, as shown below:

$$q_{300} = q_w \left( \frac{T_r - 300}{T_r - T_w} \right) \tag{17}$$

where  $q_{300}$  is the cold wall heat flux with a wall temperature of 300 K,  $T_r$  is the combustion gas flow temperature,  $T_w$  is the hot wall temperature, and  $q_w$  is the hot wall heat flux.

When processing the experimental results, the 300 K cold wall heat flux values of five working conditions were calculated, and the calculation results are shown in Table 7.

Table 7. Calculation conditions of cold wall heat flux.

No.	Test Conditions		Gardon Heat Flux Meter		Cold Wall Heat Flux of 300 K (MW/m <sup>2</sup> )
	Ma	Gas Temperature (K)	Temperature (K)	Stagnation Point Heat Flux (MW/m <sup>2</sup> )	
1	0.35	1648	366	2.14	2.255
2	0.36	1722	370	2.26	2.38
3	0.37	1814	377	2.42	2.55
4	0.38	1915	384	2.59	2.732
5	0.39	1995	466	2.73	3.026

Firstly, whether in the numerical simulation or experiment, the specimen was flat, as shown in Figure 2. Therefore, whether in the numerical simulation or experiment, the influence of blockage could be ignored. Secondly, because we only cared about the heat flux of the specimen, the pressure distribution and velocity distribution at the nozzle outlet were not recorded and discussed. However, during the experiment, due to the limitations of the existing conditions, only a small area in the center of the Gardon heat flux meter was measured, which is about the area within the red circle as shown in Figure 24, and the average heat flux value was finally taken.

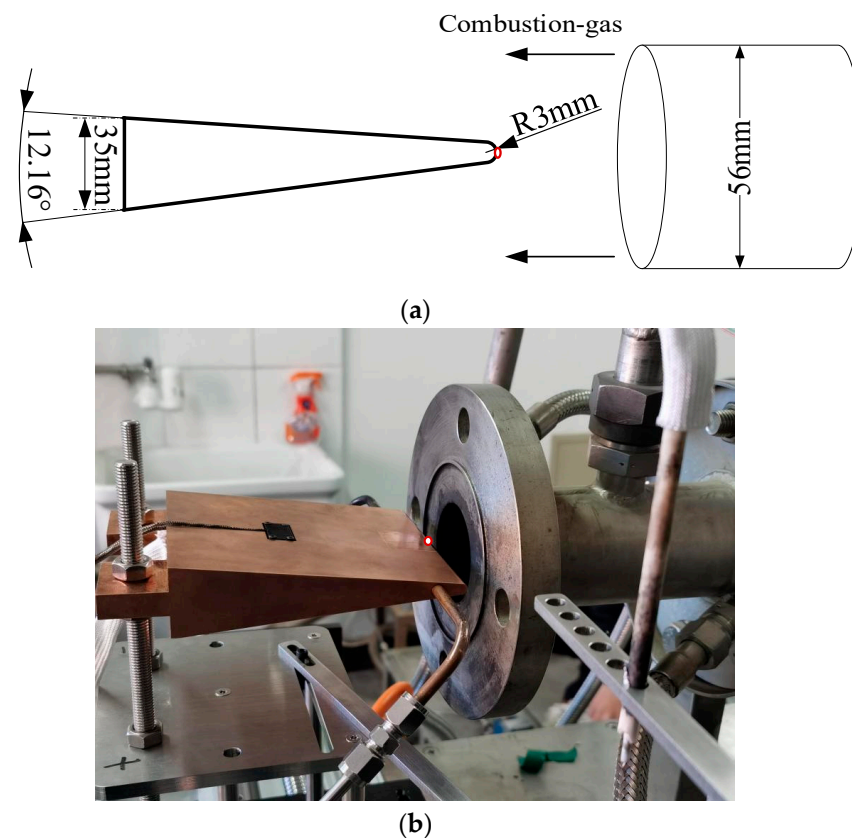


**Figure 24.** Measurement area of heat flux in the sharp wedge specimen: (a) schematic diagram; (b) actual picture.

### 5.3. Verification of the Stagnation Point Heat Flux Simulation Ability of SHCH

The comparison between the range of heat flux obtained through the test and the simulated heat flux at the stagnation point at hypersonic Mach numbers is shown in Table 8 and Figure 25.

**Table 8.** The specific test data of simulated and experimental results.

No.	Hypersonic Conditions		Gas Temp K	Experimental Results				Deviation	
	Ma	STP CW HFlux		Gas Temp K	STP Temp K	STP HFlux MW/m <sup>2</sup>	STP CW HFlux MW/m <sup>2</sup>	Gas Temp K	CW HFlux %
		MW/m <sup>2</sup>							
1	5.0	1.96	1697	1648	366	2.14	2.255	−49	+13.1
2	5.1	2.11	1764	1722	370	2.26	2.38	−42	+11.3
3	5.2	2.29	1844	1814	377	2.42	2.55	−30	+10.2
4	5.3	2.47	1923	1915	384	2.59	2.732	−8	+9.6
5	5.4	2.66	2008	1995	466	2.73	3.026	−13	+12.1

Temp—Temperature; STP—Stagnation point; HFlux—Heat flux; CW—Cold wall.

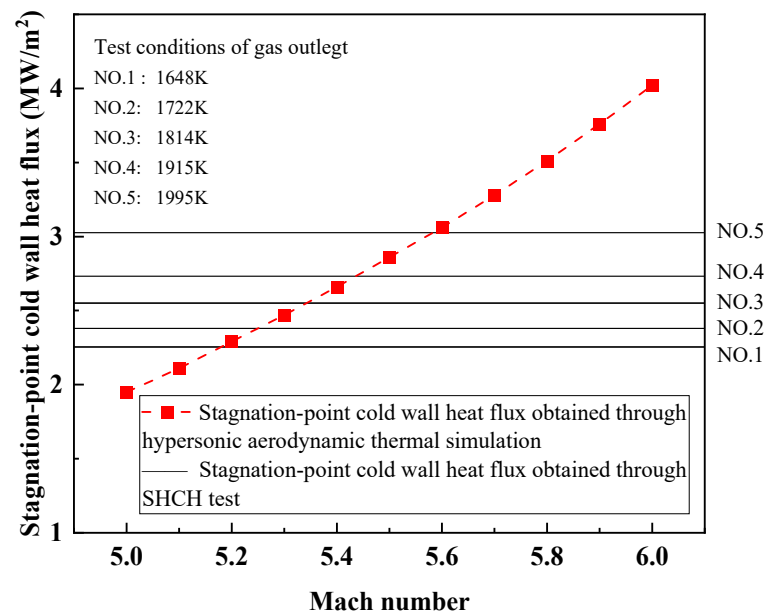


**Figure 25.** Comparison between simulated and experimental values of combustion gas heating methods.

It can be seen from Table 8 that under combustion gas temperatures of 1648 K to 1995 K, obtained by adjusting the fuel mass flow, the heat flux of the cold wall measured by the Gardon heat flux meter at the sharp wedge leading edge ranged from 2255 to 3026 kW/m<sup>2</sup>.

It can be seen from Figure 25 that the test method with 1995 K could realize the simulation of heat flux at the stagnation point at a Mach number of 5.6. At the same time, by adjusting the gas flow temperature, the hypersonic aerodynamic thermal simulation requirements could be achieved at a lower Mach number.

Due to the limitations of the stability of the test conditions, there was a certain deviation between the experimental results of gas flow temperature and the optimal target temperature value, with a maximum deviation of 49 K. However, the deviation was acceptable.

The stationary heat flux agreed well to the target heat flux, with a relative error ranging from 9.6% to 13.1%. This validated the feasibility of the surrogate model and simulation provided in Sections 4.2 and 4.3.

During the experiment, the gas temperature was lower than the optimal result, while the measured stagnation point heat flux was higher than the target value. This indicated that under certain gas temperature conditions, the actual experimental results yielded a higher stagnation point heat flux than what was obtained using numerical simulation methods. This was mainly because of factors such as high-temperature gas flow radiation in the actual experimental process, which caused the heat flux to be much larger than the numerical calculation results, which will be discussed in the next section.

#### 5.4. Verification of the Accuracy of Numerical Simulation of High-Temperature Gas Flow

Using numerical calculation methods, the actual experimental gas flow rate and temperature were used as the boundary conditions to calculate and obtain the cold wall heat flux value, which was then compared with the experimental values in Table 7, as shown in Figure 26. From the results, it can be seen that as the gas temperature increased, the stagnation point heat flux gradually increased, and the experimental values were always greater than the simulated values. The overall error remained between 9.6% and 12.2%, and the accuracy was acceptable.

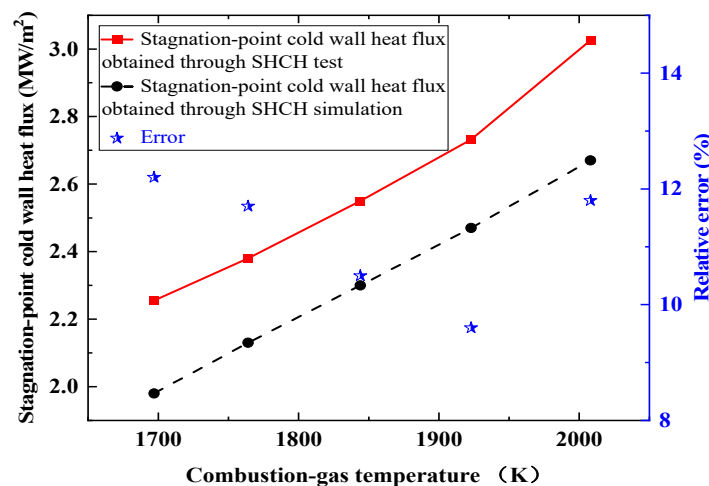


Figure 26. Comparison between simulated and experimental values of gas heating methods.

The error is derived from three aspects:

- (1) The numerical simulations did not account for the radiation from the combustion gas flow. In the CFD numerical simulation of ground gas flow, the outer surface of the sharp wedge was set to 300 K, and the obtained heat flux was the 300 K cold wall heat flux. At this time, the heat radiating outward was relatively small, and the radiation model was not opened because of its complexity. In the actual test process, the wall temperature gradually rose and finally converted into the 300 K cold wall heat flux, so radiation heat transfer was considered in the test process. However, in reality, due to the presence of moisture molecules in the combustion products of fuel at higher temperatures, there is a certain radiative capability under high-temperature conditions. Therefore, in the comparison between the simulation and experimental results, the experimental results were higher.
- (2) During the test, the leading edge of the sharp wedge was very close to the nozzle, and the surroundings of the test piece were enveloped by the gas flow. In this region, some combustion reactions might have occurred within the gas flow, leading to an enhancement in the actual heat capability. Such complex scenarios were not considered in the numerical simulations. Another factor is that the heat dissipation environment near the stagnation point differed in the simulations, as the outlet consisted of a predetermined temperature airflow devoid of any combustion process. However, in practical experiments, the stagnation point was enveloped by gas flames, potentially still harboring combustion reactions. The heat dissipation conditions might have been poor, leading to larger measured heat flux values.
- (3) As mentioned above, the actual measurement results of the Gardon heat flux meter corresponded to the average heat flux in the arc area, which was very small near the stagnation point and should be lower than the stagnation point heat flow value, in theory. The measured results were higher than the numerical simulation results of the stagnation point heat flux, which showed that the deviation from the numerical simulation results should be slightly increased on the current basis.

## 6. Conclusions

In this paper, a subsonic high-temperature combustion gas heating method is designed that can simulate the aerodynamic thermal environment of a hypersonic vehicle and satisfies the simulation target of stagnation point heat flux under hypersonic conditions.

The Kriging surrogate model is used to establish an approximate fitting relationship between the stagnation point heat flux and experimental parameters under SHCH conditions. The corresponding combustion gas temperature values are found, respectively, with the hypersonic aerodynamic heat flux at Mach 5.0~5.4 as the target value.

An experimental specimen with a Gardon heat flux meter is designed and stagnation point heat flux testing of low-speed and high-temperature combustion gas is performed at different combustion gas temperatures. When the combustion gas temperature and Mach number are 1995 K and 0.40, respectively, the measured cold wall heat flux is about 3.026 MW/m<sup>2</sup>. The results show that the measured heat flux value can realize the simulation of heat flux at the stagnation point at a Mach number of 5.6. At the same time, by adjusting the gas flow temperature, the hypersonic aerodynamic thermal simulation requirements can be achieved at a lower Mach number. The experimental results fully verify the heat simulation testing ability of subsonic high temperature combustion gas, providing a new idea for hypersonic aerothermal simulation testing.

In view of the experimental method with SHCH proposed in this paper, there are still two limitations, which are the focus of future research. The first limitation is that in the numerical simulations in this paper, whether hypersonic or ground test CFD numerical simulation, the heat flux of the sharp wedge head was the focus of attention, while the velocity gradient in the boundary layer, pressure, enthalpy, and other parameters were not recorded and discussed. The second limitation is that in the ground gas test and ground CFD numerical simulation, the composition of the gas produced by the mixture of kerosene and air combustion was completely different from that produced by the hypersonic vehicle flying in the air, but this issue was not considered and explored in detail in this article.

**Author Contributions:** Conceptualization, S.D.; methodology, R.W.; software, F.L.; validation, B.Q.; formal analysis, S.D.; investigation, Y.Z.; resources, F.L.; data curation, R.W.; writing—original draft preparation, F.L.; writing—review and editing, B.Q.; visualization, R.A.; supervision, S.D.; project administration, R.A.; funding acquisition, R.W. All authors have read and agreed to the published version of the manuscript.

**Funding:** The National Natural Science Foundation of China (Grant No. 11902026).

**Data Availability Statement:** No data can be used.

**Conflicts of Interest:** The authors declare that there are no conflict of interest regarding the publication of this paper.

## References

1. Lou, F.; Dong, S.; Ma, Y.; Qi, B.; Zhu, K. Numerical study of the influence of coupling interface emissivity on aerogel metal thermal protection performance. *Gels* **2021**, *7*, 250. [[CrossRef](#)]
2. Huang, W.; Yan, L.; Liu, J.; Jin, L.; Tan, J. Drag and heat reduction mechanism in the combinational opposing jet and acoustic cavity concept for hypersonic vehicles. *Aerosp. Sci. Technol.* **2015**, *42*, 407–414. [[CrossRef](#)]
3. Mashaei, P.; Shahryari, M.; Madani, S. Analytical study of multiple evaporator heat pipe with nanofluid; A smart material for satellite equipment cooling application. *Aerosp. Sci. Technol.* **2016**, *59*, 112–121. [[CrossRef](#)]
4. Qin, Q.; Xu, J. Numerical evaluation of aerodome and cooling jet for aero heating reduction. *Aerosp. Sci. Technol.* **2019**, *86*, 520–533. [[CrossRef](#)]
5. Rivier, M.; Lachaud, J.; Congedo, P. Ablative thermal protection system under uncertainties including pyrolysis gas composition. *Aerosp. Sci. Technol.* **2019**, *84*, 1059–1069. [[CrossRef](#)]
6. Zhu, L.; Li, Y.; Chen, X.; Li, H.; Li, W.; Li, C. Hypersonic flow characteristics and relevant structure thermal response induced by the novel combined spike-aerodome and lateral jet strategy. *Aerosp. Sci. Technol.* **2019**, *95*, 105459. [[CrossRef](#)]
7. Kuznetsov, A.; Lunev, V. Heating of a Sharp Slender Wedge in Supersonic Flow. *Fluid Dyn.* **2021**, *56*, 116–120. [[CrossRef](#)]
8. Mao, X.; Cao, W. Prediction of hypersonic boundary layer transition on sharp wedge flow considering variable specific heat. *Appl. Math. Mech.* **2014**, *35*, 143–154. [[CrossRef](#)]
9. Kasen, S.; Wadley, H. Heat Pipe Thermal Management at Hypersonic Vehicle Leading Edges: A Low Temperature Model Study. *J. Therm. Sci. Eng. Appl.* **2019**, *11*, 061001. [[CrossRef](#)]
10. Li, S.; Huang, W.; Lei, J.; Wang, Z. Drag and heat reduction mechanism of the porous opposing jet for variable blunt hypersonic vehicles. *Int. J. Heat Mass Transf.* **2018**, *126*, 1087–1098. [[CrossRef](#)]
11. Zhang, R.; Huang, W.; Li, L.; Yan, L.; Moradi, R. Drag and heat flux reduction induced by the pulsed counterflowing jet with different periods on a blunt body in supersonic flows. *Int. J. Heat Mass Transf.* **2018**, *127*, 503–512. [[CrossRef](#)]
12. Wang, Z.; Sun, X.; Huang, W.; Li, S.; Yan, L. Experimental investigation on drag and heat flux reduction in supersonic/hypersonic flows: A survey. *Acta Astronaut.* **2016**, *129*, 95–110. [[CrossRef](#)]
13. Ou, M.; Yan, L.; Huang, W.; Li, S.; Li, L. Detailed parametric investigations on drag and heat flux reduction induced by a combinational spike and opposing jet concept in hypersonic flows. *Int. J. Heat Mass Transf.* **2018**, *126*, 10–31. [[CrossRef](#)]

14. Reddy, D.; Saikia, B.; Sinha, K. Effect of High-Enthalpy Air Chemistry on Stagnation Point Heat Flux. *J. Thermophys. Heat Transf.* **2014**, *28*, 356–359. [[CrossRef](#)]
15. Rocher, M.; Hermann, T.; McGilvray, M. Correlation for Species Concentration on a Hypersonic Stagnation Point with Mass Injection. *AIAA J.* **2022**, *60*, 2798–2809. [[CrossRef](#)]
16. Ju, S. Study on Testing Environment Simulation Method for Thermal Flux Density of Aerothermal. *J. Phys. Conf. Ser.* **2019**, *1267*, 012065.
17. Simonenko, E.P.; Simonenko, N.P.; Gordeev, A.N.; Papyrov, E.K.; Shichalin, O.O.; Kolesnikov, A.F.; Avramenko, V.A.; Sevastyanov, V.G.; Kuznetsov, N.T. Study of the Thermal Behavior of Wedge-Shaped Samples of HfB<sub>2</sub>-45 vol % SiC Ultra-High-Temperature Composite in a High-Enthalpy Air Flow. *Russ. J. Inorg. Chem.* **2018**, *63*, 421–432. [[CrossRef](#)]
18. Monteverde, F.; Savino, R. ZrB<sub>2</sub>-SiC Sharp Leading Edges in High Enthalpy Supersonic Flows. *J. Am. Ceram. Soc.* **2012**, *95*, 2282–2289. [[CrossRef](#)]
19. Yang, J.; Liu, M. A wall grid scale criterion for hypersonic aerodynamic heating calculation. *Acta Astronaut.* **2017**, *136*, 137–143. [[CrossRef](#)]
20. Liu, J.; Hou, Z.; Ding, G.; Chen, X.; Chen, X. Numerical and experimental study on waverider with blunt leading edge. *Comput. Fluids* **2013**, *84*, 203–217. [[CrossRef](#)]
21. Lees, L. Laminar Heat Transfer Over Blunt-Nosed Bodies at Hypersonic Flight Speeds. *J. Jet Propuls.* **1956**, *26*, 259–269. [[CrossRef](#)]
22. Fay, J.; Riddell, F. Theory of Stagnation Point Heat Transfer in Dissociated Air. *J. Aerosp. Sci.* **1958**, *25*, 73–85. [[CrossRef](#)]
23. Regan, F.; Anandakrishnan, S. *Dynamics of Atmospheric Re-Entry*; American Institute of Aeronautics and Astronautics Press: Reston, VA, USA, 1993.
24. Singh, N.; Schwartzentruber, T. Heat flux correlation for high-speed flow in the transitional regime. *J. Fluid Mech.* **2016**, *792*, 981–996. [[CrossRef](#)]
25. Gross, E.; Jackson, E. Kinetic models and the linearized Boltzmann equation. *Phys. Fluids* **1959**, *2*, 432–441. [[CrossRef](#)]
26. Mott-Smith, H. The Solution of the Boltzmann Equation for a Shock Wave. *Phys. Rev.* **1951**, *82*, 885–892. [[CrossRef](#)]
27. Bhatnagar, P.; Gross, E.; Krook, M. A Model for Collision Processes in Gases. I. Small Amplitude Processes in Charged and Neutral One-Component Systems. *Phys. Rev.* **1954**, *94*, 511–525. [[CrossRef](#)]
28. Xiao, F.; Li, Z.; Zhang, Z.; Zhu, Y.; Yang, J. Hypersonic Shock Wave Interactions on a V-Shaped Blunt Leading Edge. *AIAA J.* **2018**, *56*, 356–367. [[CrossRef](#)]
29. Li, B.; Bao, L.; Tong, B. Physical criterion study on forward stagnation point heat flux CFD computations at hypersonic speeds. *Appl. Math. Mech.* **2010**, *31*, 839–850. [[CrossRef](#)]
30. Dong, S.; Li, Z. Research on the combined heating method using dual subsonic gas flow of high and middle temperature for thermal test of tip wedge structure. In Proceedings of the 18th AIAA/3AF International Space Planes and Hypersonic Systems and Technologies Conference, Tours, France, 24–28 September 2012.
31. Kolesnikov, A. Conditions of simulation of stagnation point heat transfer from a high-enthalpy flow. *Fluid Dyn.* **1993**, *28*, 131–137. [[CrossRef](#)]
32. Kolesnikov, A. The concept of local simulation for stagnation point heat transfer in hypersonic flows—Applications and validation. In Proceedings of the 21st Aerodynamic Measurement Technology and Ground Testing Conference, Denver, CO, USA, 19–22 June 2000.
33. Yang, S.; Tao, W. *Heat Transfer*; Higher Education Press: Beijing, China, 2014.
34. Wang, W.; Qian, W.; Bai, Y.; Wang, K. Numerical studies on the thermal-fluid-structure coupling analysis method of hypersonic flight vehicle. *Therm. Sci. Eng. Prog.* **2023**, *40*, 101792. [[CrossRef](#)]
35. Lou, F.; Dong, S.; Zhao, B.; Qi, B. Structure design and performance test of a high temperature combustor based on combustion-gas wind tunnel device. *Heat Transf. Res.* **2022**, *53*, 21–36. [[CrossRef](#)]
36. A, R.; Qi, B.; Chen, X.; Wang, R.; Song, S.; Zhou, Y. Parameter optimization of dual gas flow combined thermal test based on surrogate model. *J. Aerosp. Power* **2023**, *38*, 2097–2106.
37. Xiong, K.; Li, Y.; Dong, S. Temperature distribution of a test specimen with high-speed heat airflow passing through. *Therm. Sci.* **2018**, *22*, 2527–2538. [[CrossRef](#)]
38. Simpson, T.W.; Mauery, T.M.; Korte, J.J.; Mistree, F. Kriging Models for global approximation in simulation-based multidisciplinary design optimization. *AIAA J.* **2001**, *39*, 2233–2241. [[CrossRef](#)]

**Disclaimer/Publisher’s Note:** The statements, opinions and data contained in all publications are solely those of the individual author(s) and contributor(s) and not of MDPI and/or the editor(s). MDPI and/or the editor(s) disclaim responsibility for any injury to people or property resulting from any ideas, methods, instructions or products referred to in the content.